Imaging poly(ADP-ribose) polymerase-1 (PARP1) in vivo with ^{18}F-labeled brain penetrant positron emission tomography (PET) ligand

Xin Zhou,[1,#] Jiahui Chen,[1,#] Jimmy S. Patel,[1,2,#] Wenqing Ran,[3] Yinlong Li,[1] Richard S. Van,[4] Mostafa M. H. Ibrahim,[5] Chunyu Zhao,[1] Yabiao Gao,[1] Jian Rong,[1] Ahmad F. Chaudhary,[1] Guocong Li,[3] Junqi Hu,[3] April T. Davenport,[6] James B. Daunais,[7] Yihan Shao,[4] Chongzhao Ran,[8] Thomas L. Collier,[1] Ahmed Haider,[1] David M. Schuster,[1] Allan Levey,[9] Lu Wang,[3] Gabriel Corfas[5] and Steven H. Liang[1,*]

[1]*Department of Radiology and Imaging Sciences, Emory University, Atlanta, Georgia 30322, United States.*

[2]*Department of Radiation Oncology, Winship Cancer Institute of Emory University, Atlanta, Georgia 30322, United States.*

[3]*Center of Cyclotron and PET Radiopharmaceuticals, Department of Nuclear Medicine & Key Laboratory of Basic and Translational Research on Radiopharmaceuticals, The First Affiliated Hospital of Jinan University, Guangzhou, 510630, China*

[4]*Department of Chemistry and Biochemistry, University of Oklahoma, Norman, Oklahoma 73019, United States.*

[5]*Kresge Hearing Research Institute, Department of Otolaryngology-Head and Neck Surgery, University of Michigan, Ann Arbor, Michigan 48109, United States.*

[6]*Department of Physiology and Pharmacology, Wake Forest School of Medicine, Winston Salem, North Carolina, 27157, United States.*

[7]*Department of Internal Medicine, Section on Infectious Diseases, Wake Forest School of Medicine, Winston Salem, North Carolina, 27157, United States.*

[8]*Athinoula A. Martinos Center for Biomedical Imaging, Department of Radiology, Massachusetts General Hospital and Harvard Medical School, Boston, Massachusetts, 02114, United States.*

[9]*Department of Neurology, Emory University, Atlanta, Georgia 30322, United States.*

ABSTRACT:

Poly(ADP-ribose) polymerase 1 (PARP1) is a multifunctional protein involved in diverse cellular functions, notably DNA damage repair. Pharmacological inhibition of PARP1 holds potential therapeutic benefits for various pathologies. Despite the current FDA approval of PARP inhibitors, challenges persist in achieving PARP1 selectivity and effective blood-brain barrier (BBB) penetration. The development of a PARP1-specific positron emission tomography (PET) ligand is crucial for disease biology and target occupancy studies, aiding the development of PARP1-specific inhibitors. In this study, we leverage the recently identified PARP1 inhibitor, AZD9574, to introduce the design and development of its ^{18}F-isotopologue ([^{18}F]**5**). Our comprehensive approach, encompassing pharmacological, cellular, autoradiographical, and in vivo PET imaging, demonstrates the capacity of [^{18}F]**5** for specific binding to PARP1 and successful penetration of the BBB. These findings position [^{18}F]**5** as a viable molecular imaging tool, poised to facilitate the exploration of physio-pathological changes of PARP1 across various diseases.

Keywords: Poly(ADP-ribose) polymerase-1 (PARP1); DNA damage; Cell death; Positron emission tomography (PET); Fluorine 18

INTRODUCTION

Poly (ADP-ribose) polymerases (PARPs) constitute a family of enzymes that play an integral role in DNA repair and are found in a variety of tissues.[1] Among this family of 18 related members, PARP1 and PARP2 are the most abundant and have specific functions in genome surveillance and DNA repair pathways.[2] PARP1, in particular, uniquely binds to single-stranded DNA breaks and initiates repair by synthesizing a poly (ADP-Ribose) polymer.[3] The role of PARP1 in DNA repair is intriguing, as certain tumors with defects in homologous recombination mechanisms may depend on PARP1-mediated DNA repair for survival, rendering them susceptible to PARP inhibition.[1] Olaparib, the pioneering PARP1/2 inhibitor, gained FDA approval in 2014 for treating ovarian cancer with a germline BRCA mutation.[4] Subsequently, Rucaparib and Niraparib received approval for ovarian cancer treatment in 2016 and 2017, respectively. Olaparib garnered further FDA approval in 2022 for treating high-risk early breast cancer and in 2023 for BRCA-mutated metastatic castration-resistant prostate cancer.[5, 6] Beyond cancer, PARP inhibitors have shown promise in various inflammatory disorders, including arthritis, psoriasis, colitis, asthma, diabetic complications, as well as cardiovascular and neurodegenerative diseases.[7, 8] The benefit of PARP inhibition in non-oncologic applications primarily stems from inhibition of PARP-mediated pro-inflammatory and apoptotic signaling pathways which, as an example, has been seen during neurologic ischemic and ischemic-reperfusion injury.[9-11] While prospective randomized studies remain to be performed, PARP inhibitors have demonstrated neuroprotective effects in response to stress in preclinical models, thereby underscoring the broad therapeutic potential of PARP inhibition.[12-15]

Positron emission tomography (PET) is a widely-utilized functional imaging technique that allows for the non-invasive examination of *in vivo* physiopathology through the use of radioactive ligands.[16-18] The most common and widely utilized radioactive isotope for PET imaging is fluorine 18 (^{18}F).[19-21] Over the past decade, numerous PARP targeted radiotracers have emerged and been recently reviewed.[18, 22-24] Notable among these is [^{18}F]FluorThanatrace ([^{18}F]FTT), which has undergone first-in-human imaging studies and validated its efficacy as a biomarker for quantifying PARP expression levels, particularly in breast and

ovarian cancer patients.[25] Additionally, [^{18}F]PARP-inhibitor ([^{18}F]PARPi) has been identified as a safe and feasible radiotracer for imaging head and neck cancers.[26] Furthermore, preclinical evaluation of [^{18}F]Olaparib demonstrated uptake in pancreatic cell tumors, in vitro and within xenograft models.[27] Despite the significant progress in the development of various PARP1 radiotracers, a prevalent limitation persists in their restricted ability to penetrate the blood-brain-barrier.[11] This constraint impedes the assessment of PARP1-specific expression and distribution in the brain, particularly in conditions such as glioma, brain metastasis and other central nervous system (CNS) diseases involving with DNA damage/cell death. Furthermore, many of these ligands are derivatives of PARP1/2 non-selective inhibitors, such as rucaparib and olaparib, emphasizing the need for new PET ligands with high selectivity for PARP1 over PARP2.

Recent advancements in PARP-targeted PET imaging include the discovery of a novel ^{11}C-labeled veliparib derivative, [^{11}C]PyBic, which demonstrates encouraging brain permeability in rodents and nonhuman primates (NHPs).[28] However, its selectivity for PARP1 over PARP2 requires further demonstration due to its origin from veliparib, which is nearly equipotent against both PARP1 and PARP2. Concurrently, Schou and colleagues have disclosed another PET tracer designed to target PARP1, known as [^{11}C]AZ14193391, in recent conference abstracts.[29, 30] The tracer exhibits promising capability in penetrating the CNS, albeit with an unconventional brain pharmacokinetic profile characterized by an upward time-activity curve in the later timepoints. Importantly, the use of ^{11}C-labeled radiotracers typically necessitates an onsite cyclotron due to the shorter half-life ($t_{1/2}$ = 20.4 min), thereby constraining its broad clinical application and commercialization. All these aforementioned challenges accentuate continuous efforts and urgent need to enhance both PARP1 selectivity and practicality of PET tracers for improved imaging precision and wider clinical utility.

Inspired by the recent disclosure of AZD9574,[31] a fluorine-containing PARP1 therapeutic agent distinguished by its exceptional potency, selectivity and favorable ADME properties, we postulated that an ^{18}F-isotopologue of AZD9574 may hold promise as a PARP1-selective PET ligand with the ability to penetrate the brain. Through the strategic drug repurposing of AZD9547, presently undergoing Phase I

clinical trials as a therapeutic agent, into a diagnostic molecular imaging PET probe, we anticipate a streamlined translation of PET imaging to clinical research applications. In this work, we describe the radiolabeling strategy, precursor synthesis, pharmacological and ADME characterization of the proposed PET ligand. Furthermore, we provide in-depth *in vitro* validation through cellular uptake and autoradiography studies, as well as *in vivo* PET evaluations in NHPs, supporting the potential clinical utility of our approach.

RESULTS AND DISCUSSION

Chemistry. The process of ^{18}F-isotopologue labeling involves the incorporation of ^{18}F radionuclide into the molecule of interest without altering its original structure.[16] AZD9574 (6-fluoro-5-(4-((5-fluoro-2-methyl-3-oxo-3,4-dihydroquinoxalin-6-yl)methyl)piperazin-1-yl)-N-methylpicolinamide; compound **5**; Figure 1) contains two fluorine atoms, with one strategically positioned in a favorable meta position of the corresponding picolinamide scaffold. The electron-deficient nature of the pyridine core in the picolinamide provides a conducive environment for S_NAr reactions without the need for an activation group.[20] As a result, we designed a brominated analog, 6-bromo-5-(4-((5-fluoro-2-methyl-3-oxo-3,4-dihydroquinoxalin-6-yl)methyl)piperazin-1-yl)-N-methylpicolinamide (compound **8**), to serve as the corresponding labeling precursor. The synthesis pathways for our key compound **5** and its bromo counterpart **8** are depicted in Figure 1. Both compounds share a common synthetic route and were efficiently derived from commercially available methyl 5-bromo-6-fluoropicolinate (**1**) and methyl 6-bromo-5-fluoropicolinate (**6**), respectively. In the synthesis of compound **5**, the key intermediate **2** was synthesized through a Pd-catalyzed Buchwald-Hartwig C-N coupling reaction between 5-bromo-6-fluoropicolinate (**1**) and tert-butyl piperazine-1-carboxylate (**2**), yielding a satisfactory 56% yield. Subsequently, Boc deprotection was achieved by the addition of HCl in 1,4-dioxane. The resulting amine underwent reaction with 7-(bromomethyl)-8-fluoro-3-methylquinoxalin-2(1H)-one (**4**) and triethylamine. Finally, an amine-ester exchange was performed, yielding compound **5** with 55% yield. Similarly, the radiolabeling precursor compound **8** was prepared by

starting from methyl 6-bromo-5-fluoropicolinate (**6**). The Boc-protected amine intermediate **7** was obtained through aromatic nucleophilic substitution with Boc-protected piperazine in 56% yield. Following analogous steps of Boc deprotection, treatment with 7-(bromomethyl)-8-fluoro-3-methylquinoxalin-2(1H)-one (**4**), and amine-ester exchange with methylamine, compound **8** was obtained in 64% yield. In all, compound **5** and its brominated labeling precursor, compound **8**, were synthesized from their corresponding methyl picolinates in four steps with an overall yield of 6% and 8%, respectively.

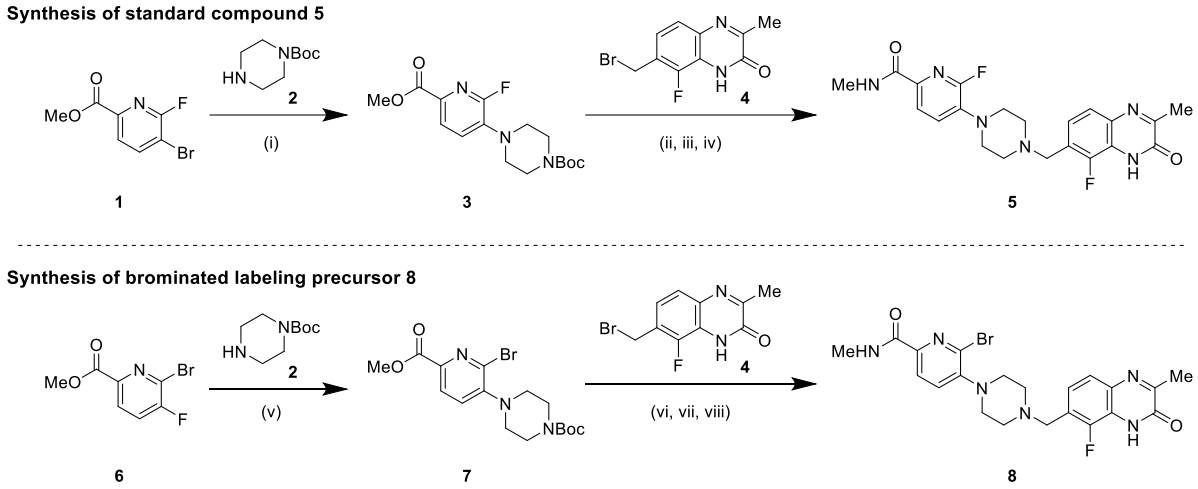

Figure 1. Synthesis of compound **5** and its brominated labeling precursor compound **8**. Conditions: (i) *N*-Boc piperazine, Pd-RuG3, Cs_2CO_3, 1,4-dioxane, 100°C, 24 h, 56%; (ii) HCl in 1,4-dioxane (3 mol/L), 6 h, rt, used without purification; (iii) DIPEA, MeCN, 80°C, 12 h, 20%; (iv) $MeNH_2$ in THF (2 mol/L), EtOH, 80°C, 12 h, 55%; (v) K_2CO_3, DMF, 130°C, 48%; (vi) HCl in 1,4-dioxane (3 mol/L), 6 h, rt, used without purification; (vii) DIPEA, MeCN, 80°C, 12 h, 26%; (viii) $MeNH_2$ in THF (2 mol/L), EtOH, 80°C, 12 h, 64%.

Pharmacology. The pharmacology, physiochemical and ADME properties of compound **5** are summarized in **Table 1**. To validate the potency and selectivity of compound **5** against PARP1, we performed enzymatic assays using commercially available PARP1 and PARP2 testing kits (see supplementary information). Compound **5** exhibited high potency against PARP1 with a low IC_{50} value of 1.20 nM, while demonstrating low potency against PARP2 with an IC_{50} value exceeding 1.0 μM. This showcased a greater than 800 fold selectivity toward PARP1 over PARP2. Compound **5** exhibited favorable physiochemical attributes for CNS penetration, including molecular weight of 428.4, cLogP value of 1.83 and topological polar surface area (TPSA) of 89.4. The blood–brain barrier permeability (logBB) value was predicted as -0.30 using ACD/Percepta™, and the CNS MPO score was determined as 4.90, both falling within the preferred range for brain permeability.[32-34] Furthermore, an *in vitro* Pg-P efflux assay of compound **5** demonstrated high passive permeability (P_{app} AB: 42.5 × 10^{-6} cm/s) and a low efflux ratio (MDR1 BA/AB: 0.85) and lipophilicity measurement was completed by the 'shake-flask' method with $logD_{7.4}$ value of 1.87. The protein binding study indicated that compound **5** possesses reasonable unbound fractions in the plasma of various species, including rats (6.9%, free) and humans (2.6%, free). Additionally, compound **5** exhibited in vitro hERG channel safety with IC_{50} >100 μM and CellTiter-Glo luminescent cell viability assay in HepG2 cells with IC_{50} >100 μM. No significant interactions with metabolic cytochrome P450 (CYP) isoforms were identified (all major six CYP450s IC_{50} >5 μM). These favorable pharmacological and ADME properties affirmed compound **5** as the lead molecule for further evaluations.

Table 1. Pharmacology, physiochemical and ADME properties of compound **5**

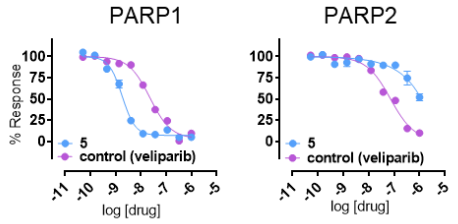

PARP1 IC_{50} (nM)	PARP2 IC_{50} (nM)	PARP1/2 selectivity
1.2	>1000	> 800

MW	clogP	logD	TPSA
428.44	1.83	1.87	89.4

LogBB	MPO score	P_{app} (A–B) ($x10^{-6}$ cm/s)	efflux ratio
-0.3	4.9	42.5	0.85

Protein binding	Mean (% free)
Human plasma	2.6
Rat plasma	6.9

CYP isoforms	IC_{50}
CYP1A2, CYP2D6, CYP2C19 CYP3A4, CYP2C9, CYP19A	all >5 μM

hERG IC_{50} (μM)	HepG2 IC_{50} (μM)
>100	>100

Molecular docking study. To elucidate the ligand-protein interaction between the lead compound **5** and PARP1, we established a homology model and performed molecular docking studies based on previously published PARP1 x-ray co-crystal structures. The structural data of PARP1 utilized in this study were retrieved from the Protein Data Bank (PDB 7ONT).[35] A favorable binding position in the catalytic domain of PARP1 (residues 788-1014) was characterized by a quinoxalin-2(1H)-one moiety interacting with residues G863, S904, and Y907, and a picolinamide moiety interacting with I879 (Figure 2A). Specifically, the quinoxalin-2(1H)-one moiety formed two hydrogen bonds with the peptide backbone of residue G863 (2.871 and 2.006 Å, respectively), and one hydrogen bond with the sidechain of residue S904 (2.912 Å). Additionally, pi-pi stacking occurred between this moiety and residue Y908 with a distance of 3.336 Å. In the loop region, a picolinamide moiety formed a hydrogen bond with the peptide backbone of residue I879 (2.133Å). The binding pose suggests the quinoxaline-2(1H)-one moiety to preferentially orient towards the hydrophobic region with the fluorinated substituent pointing toward a polar region, while the picolinamide scaffold binds a charged region within the binding pocket with its fluorinated substituted in a positively charged region (Figure 2B). This molecular docking study provides valuable insights into not only the specific interactions contributing to the binding affinity between compound 5 and PARP1, but also presents opportunities for fine-tuning molecular properties to enhance its overall characteristics.

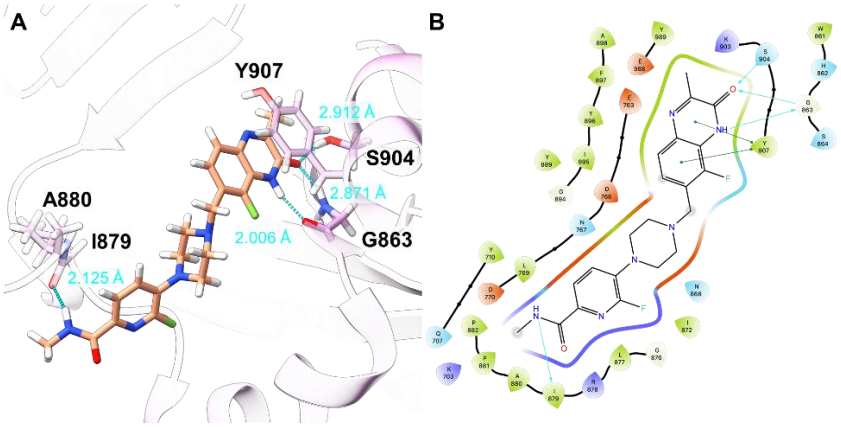

Figure 2. Molecular docking structures of compound **5** onto PARP1 (PDB ID: 7ONT). (A) 3D ligand interaction and (B) 2D interaction plot. The hydrogen bonding interactions between compound **5** and PARP1 residues are indicated by turquoise blue lines in Panel A and Panel B.

Radiochemistry. Encouraged by the promising potency, selectivity and ADME attributes, we performed the synthesis of ^{18}F-labeld isotopologue of compound **5** ([^{18}F]**5**) for further PET evaluation. As outlined in Figure 3A, radioligand [^{18}F]**5** could be synthesized via a direct S_NAr displacement reaction of the corresponding bromo precursor **8**. The radiofluorination was performed by heating the mixture of precursor 8 and azeotropically dried [^{18}F]fluoride with various bases and solvents. Initially, the radiosynthesis of [^{18}F]**5** was attempted using K_2CO_3/K_{222} system in the presence of DMF at 150 ºC for 20 min (Entry 1). Unfortunately, no desired product was observed. Similar results were obtained when switching the solvent to DMSO (Entry 2). Subsequent attempts with tetraethylammonium bicarbonate (TEAB) in DMSO as the solvent showed an increased RCY to 18% (Entry 3). However, even in the presence of increasing amount of precursor (2 mg), a lower 11% RCY was detected with DMF as the solvent at 150 ºC for 20 min (Entry 4). This suggested that S_NAr reactions of compound **8** proceeded well, preferably in DMSO. Consequently, a higher temperature was applied when DMSO was used as the solvent, resulting in 25% RCY (Entry 5). In addition, reducing the precursor loading to 0.5 mg resulted in a slightly lower RCY (Entry 6). As a result, under the optimal conditions (Entry 5), compound [^{18}F]**5** was obtained with 15% RCY (isolated and non-decayed) with excellent radiochemical purity (>99%) and greater than 37 GBq/μmol molar activity. Moreover, ligand [^{18}F]**5** exhibited exceptional stability (>95%) and no radiolysis in various formulation and media, including plasma and liver microsome across several species (rat, NHP, and human; Figure 3B-C; For stability in PBS, see Figure S1 in the supplementary information) within 90 min by in vitro experiments.

A.

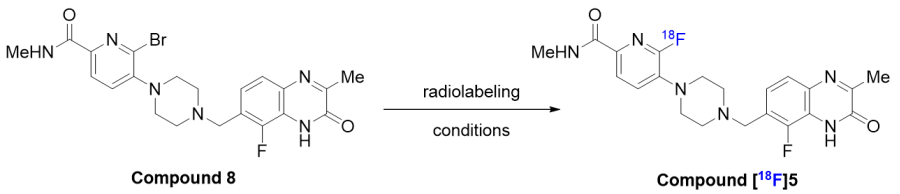

Entry	Precursor	Base	Solvent (0.5 mL)	Temperature	RCY[a]
1	1.0 mg	K_2CO_3/K_{222} (2 mg/ 10 mg)	DMF	150 °C	0
2	1.0 mg	K_2CO_3/K_{222} (2 mg/ 10 mg)	DMSO	150 °C	0
3	1.0 mg	TEAB (3 mg)	DMSO	150 °C	18%
4	2.0 mg	TEAB (3 mg)	DMF	150 °C	11%
5	1.0 mg	TEAB (3 mg)	DMSO	170 °C	25% (15%)[b]
6	0.5 mg	TEAB (3 mg)	DMSO	170 °C	22%

B.

C.

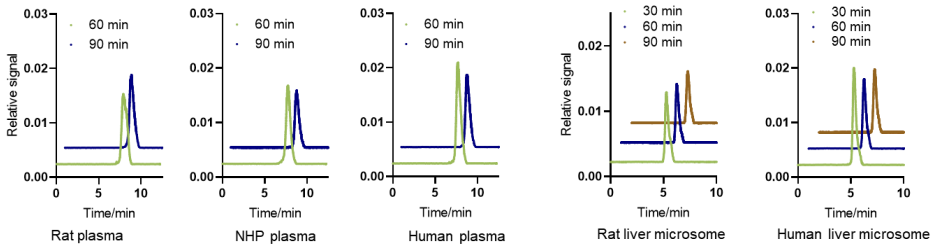

Figure 3. Radiosynthesis and optimization of **[^{18}F]5** and stability test. [a] Radiochemical yield (determined by radio-HPLC). [b] The value in parenthesis refers to an average isolated radiochemical yield (non-decay-corrected, n = 4); (B) Stability of radioligand **[^{18}F]5** in plasma; and (C) in liver microsomes of several species (rats, NHPs, and humans)

Cellular uptake studies. To assess specific binding at the cellular level, *in vitro* cell uptake assays of [^{18}F]**5** were conducted in PC3 cell lines, as shown in Figure 4. Validation of PARP1 expression was confirmed through Western blotting analysis using a commercially available PARP1 antibody (see Figure S2 in the supplementary information). The uptake of [^{18}F]**5** in PC3 cells demonstrated a rapid increase of cellular uptake within the initial 5 minutes of addition, reaching its peak at 30 minutes (Figure 4A). [^{18}F]**5** uptake displayed a dose-dependent reduction (from 12.4%-83.3% blockade) with escalating doses of compound AZD-9574 (Figure 4B). Furthermore, the PARP1 blocking reagent Olaparib significantly attenuated the uptake signal of [^{18}F]**5** (Figure 4C). In contrast, the PARP2 blocking reagent UPF-1035 exhibited no inhibitory effect on [^{18}F]**5** uptake (Figure 4D). These findings collectively affirm the robust specific binding of [^{18}F]**5** to PARP1 and excellent selectivity for PARP1 over PARP2 at the cellular level.

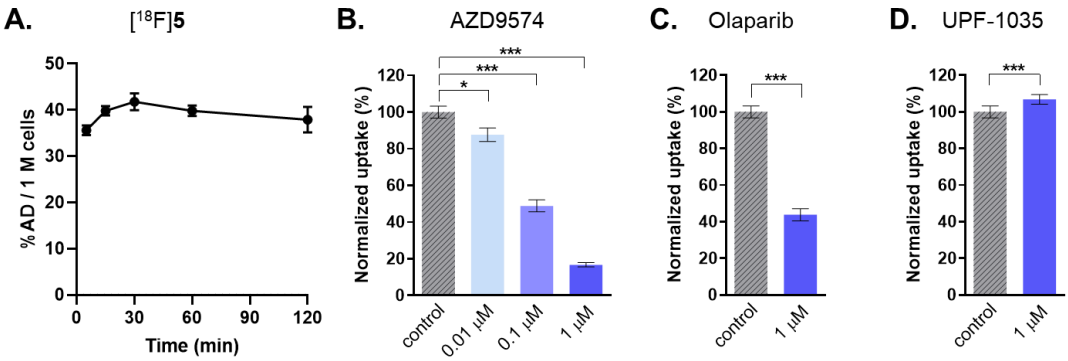

Figure 4. Cell uptake assay of [^{18}F]**5** in PC3 cell lines. (A) Cell uptake in different time points (5 min, 15 min, 30 min, 60 min and 120 min, respectively); (B) Baseline and blocking studies in the presence of AZD9574 (0.01 μM, 0.1 μM and 1 μM, respectively); (C) Baseline and blocking studies in the presence of Olaparib (1 μM); and (D) Baseline and blocking studies in the presence of UPF-1035 (1 μM), a PARP2 inhibitor. %AD = % added dose in the cell uptake assays. All data are mean ± SD, n = 3. Statistical significance was indicated as asterisks: *$p \leq 0.05$, ***$p \leq 0.001$.

In vitro autoradiography. To investigate the specific binding of **[^{18}F]5** towards PARP1, *in vitro* autoradiography was conducted on rodent and NHP brain sections (Figures 5-7). As illustrated in Figure 5A and 5B, baseline studies with **[^{18}F]5** revealed heterogeneity in radioactivity levels across various rat brain regions. The highest uptake was observed in the cerebellum and hippocampus, while the lowest uptake occurred in the pons. The radioactive distribution profile of **[^{18}F]5** corresponded with the PARP1 expression pattern in rodents. Under blocking conditions with well-known potent and selective PARP1 inhibitors (AZD2461, Olaparib, Pamiparib, Rucaparib, Veliparib, AZD9574 at 10 μM), the accumulation of radioactivity in all brain regions were significantly reduced by greater than 85% (Figure 5C). Notably, brain regions with relatively high levels of PARP1 exhibited a much higher reduction in radioactive uptake, such as the cerebellum, hippocampus and cerebral cortex. To distinguish the binding specificity of tracer **[^{18}F]5** targeting PARP1 and PARP2, a blocking study was conducted with a selective PARP2 inhibitor, UPF-1035, under 10 μM high concentration. In contrast to the significant blockade observed in the presence of other PARP1 inhibitors, UPF-1035 blocking exhibited only a modest signal reduction and displayed a heterogeneous distribution analogous to baseline conditions (Figure 5D).

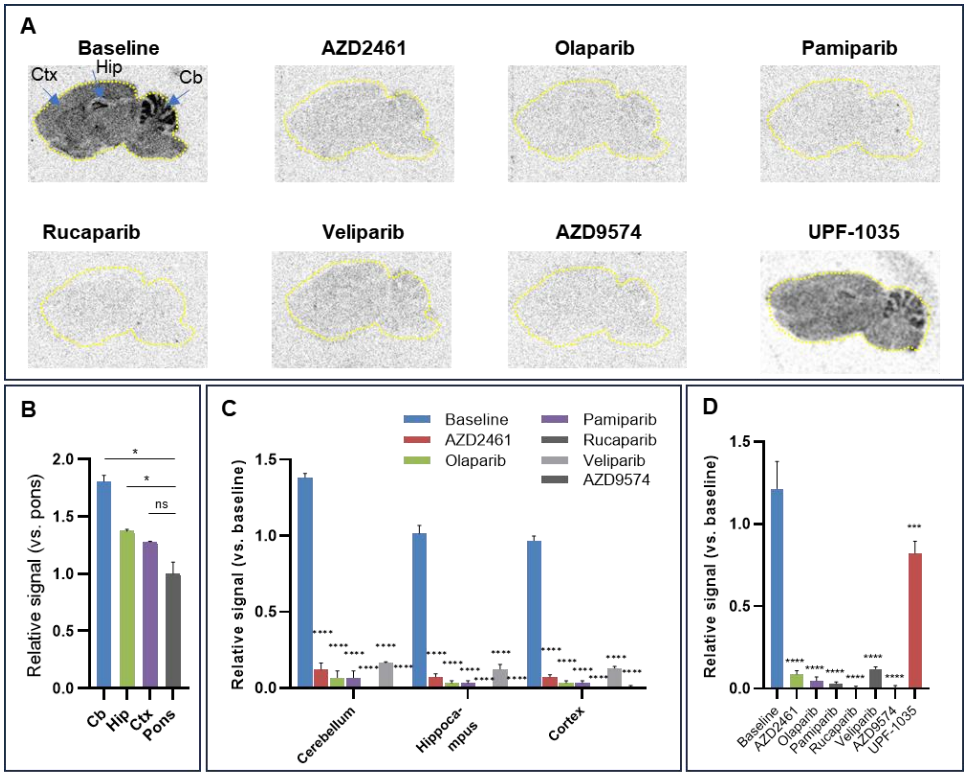

Figure 5. Autoradiography studies of radioligand **[^{18}F]5** in rat brain sections. (A) Baseline and blocking autoradiograms in the presence of PARP1 inhibitors (AZD2461, Olaparib, Pamiparib, Rucaparib, Veliparib, AZD9574) and PARP2 inhibitor (UPF-1035) at 10 μM concentration; (B) Quantification of radioactivity in different brain regions under baseline conditions, consistent with PARP1 expression profile; (C) Quantification of radioactivity uptake in regional brain sections (cerebellum, hippocampus and cortex) under baseline and blocking conditions using PARP1 inhibitors (10 μM) in panel A; and (D) Quantification of radioactivity uptake in whole brain sections under baseline and blocking conditions using PARP1 and PARP2 inhibitors (10 μM) in panel A. All data are mean ± SD, n = 3. Statistical significance was indicated as asterisks: *$p \leq 0.05$, ***$p \leq 0.001$, ****$p \leq 0.0005$, and ns = no significant. Ctx = cerebral cortex; Hip = hippocampus; Cb = cerebellum.

With promising *in vitro* autoradiography results obtained with rat brain sections, we extended our investigation to NHP brain sections (Figure 6A). In vitro autoradiography was conducted on NHP cerebellum brain sections under baseline and blocking conditions with PARP1 inhibitors (AZD9574, Olaparib), and PARP2 inhibitor UPF-1035 at the concentration of 10 μM. Similar to the outcomes observed in rat brain sections, **[^{18}F]5** exhibited high uptake in the cerebellum, with a substantial uptake reduction when pre-treated with AZD9574 and Olaparib (Figure 6B). Under blocking conditions with UPF-1035 (10 μM), radioactivity accumulations in the cerebellum showed a modest approximate 20% reduction. These results with NHP sections further support the excellent *in vitro* specific binding of **[^{18}F]5**.

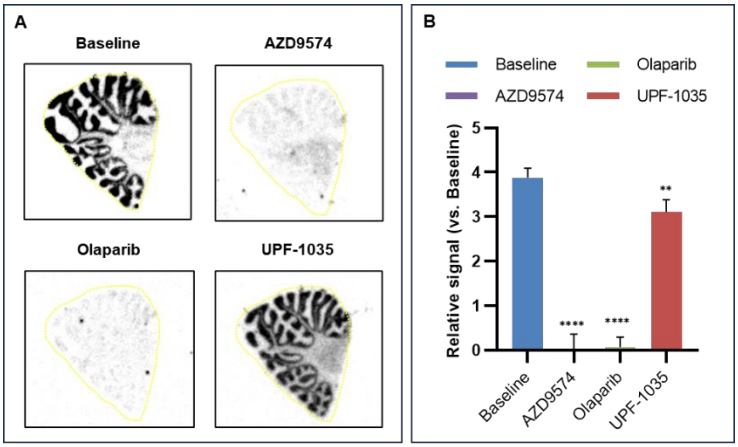

Figure 6. Autoradiography of radioligand **[^{18}F]5** in NHP cerebellum brain sections. (A) Baseline and blocking autoradiograms in the presence of PARP1 inhibitor (AZD9574, Olaparib) and PARP2 inhibitor (UPF-1035) at 10 μM concentration; and (B) Quantification of radioactivity uptake in the cerebellum under baseline and blocking conditions. All data are mean ± SD, n = 3. Statistical significance was indicated as asterisks: $^{**}p \leq 0.01$, $^{****}p \leq 0.0005$.

To further highlight the specific binding of **[^{18}F]5**, *in vitro* autoradiography was conducted using PARP1$^{(-/-)}$ knockout mice[36] and their corresponding wide-type counterpart PARP1$^{(+/+)}$. As depicted in Figure 7A, **[^{18}F]5** exhibited characteristic high uptake in the cerebellum and hippocampus in the wild-type, similar to the baseline conditions observed in rat brain sections. The radioactivity accumulation was significantly reduced by greater than 75% in the whole brain region of PARP1$^{(-/-)}$ knockout (Figure 7B). Brain regions featuring relatively high level of PARP1 expression, exhibited much higher reduction of radioactive uptake, such as the cerebellum and hippocampus as shown in Figure 7C, which is consistent with our biological validation of PARP1 expression in the mouse brain using Western blot analysis (Figure 7D). In all, autoradiograph studies conducted on rat and NHP brain tissues, coupled with validation using PARP1 knockout mouse models, clearly confirmed the high specific binding and excellent selectivity of **[^{18}F]5** across different species.

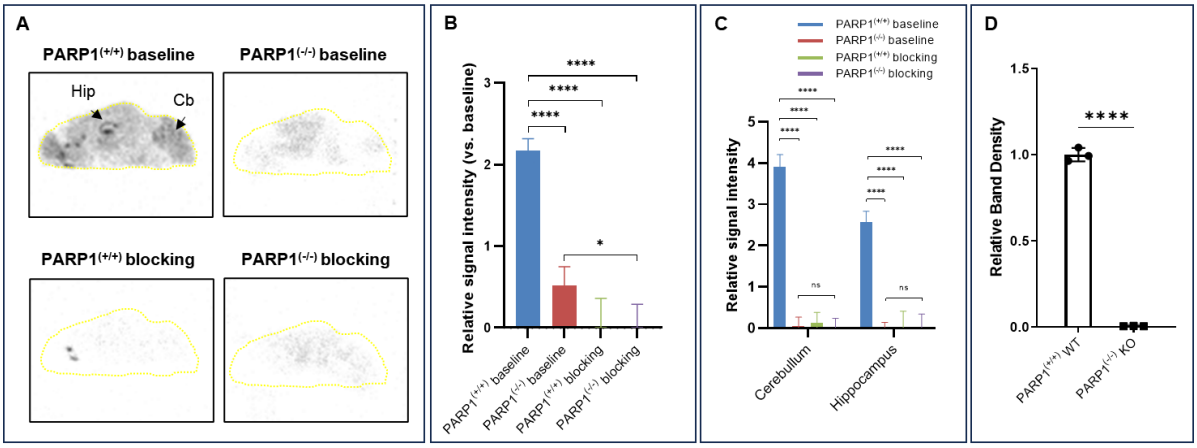

Figure 7. Autoradiography of radioligand **[^{18}F]5** in PARP1 knockout mouse brain sections. (A) Baseline and blocking autoradiograms in wild-type PARP1$^{(+/+)}$ and PARP1$^{(-/-)}$ knockout mouse brain tissues with or without with Olaparib (10 μM); (B) Quantification of radioactivity in the mouse whole brain under baseline and blocking conditions; (C) Quantification of radioactivity in the mouse cerebellum and hippocampus under baseline and blocking conditions; and (D) Quantification of PARP1 expression in wild-type PARP1$^{(+/+)}$ and PARP1$^{(-/-)}$ knockout mouse brain tissues by Western blot analysis. All data are mean ± SD, n = 3. Statistical significance was indicated as asterisks: *$p \leq 0.05$, ****$p \leq 0.0005$, and ns = no significant.

NHP PET imaging. The compelling in vitro performance and favorable ADME properties motivated us to perform a proof-of-concept evaluation of [^{18}F]**5** in a NHP PET study. PET image acquisition was initiated by the administration of ligand [^{18}F]5 (4.05 ± 0.54 mCi) for baseline ~~s~~cans. [^{18}F]**5** showed moderate-to-good brain penetration with heterogeneous radioactivity levels across various NHP brain regions. Radioactivity levels in all brain regions steadily increased up to 30 minutes post injection before plateauing. The cerebellum exhibited the highest radioactivity uptake at 1.2 SUV, followed by the prefrontal cortex (1.1 SUV), hippocampus (1.05 SUV), and caudate (0.88 SUV). The lowest radioactivity level was observed in the pons (0.67 SUV), which was concordant with the autoradiography results in rodents. To further quantify the specific binding of [^{18}F]**5**, we conducted an analysis of non-displaceable binding potential (BP_{ND}) values using a simplified reference tissue model (SRTM).[37, 38] The pons was chosen as a pseudo reference region due to its minimal brain uptake evident in TAC profiles. The BP_{ND} image and bound signal of [^{18}F]**5** in the monkey brain displayed a decreasing order in the cerebellum, hippocampus, caudate and pons under baseline conditions. This distribution pattern aligns with the known expression of PARP1 in the brain,[39] corroborated by *in vitro* autoradiography results presented in Figures 5-7.

CONCLUSION

We present the synthesis and preclinical assessment of [^{18}F]**5**, a novel PET ligand derived from the extensively studied PARP1 inhibitor, AZD9574. The synthesis of [^{18}F]**5** was efficiently achieved through a straightforward and reproducible S_NAr reaction with 21% RCY and greater than 1 Ci/μmol molar activity that supports subsequent investigations. [^{18}F]**5** demonstrated favorable pharmacological and ADME characteristics, displaying PARP1 selectivity in both cellular and radiographical studies. Furthermore, its potential was underscored by evidence of BBB penetration through NHP PET studies. These findings collectively suggest that [^{18}F]**5** holds promise as a promising candidate for future translational studies and excellent lead in medicinal chemistry for balancing potency, selectivity and brain kinetics. Further evaluation in disease models, including CNS and oncological applications, has the potential to unveil

valuable insights into the mechanistic role of PARP1 during disease progression and/or in response to therapeutic interventions.

EXPERIMENTAL SECTION

General Information. The experimental procedures were conducted as previous reports[34, 37] with minor modifications. All chemicals were purchased from commercial suppliers and used in the synthesis without further purification. The NMR spectra were collected on a 600 MHz or 400 MHz Inova spectrometer at room temperature. Specifically, ^{1}H NMR spectra, ^{13}C NMR spectra, and ^{19}F NMR spectra were obtained at 600, 152, and 376 MHz, respectively. ^{1}H NMR chemical shifts were determined relative to internal $(CH_3)_4Si$(TMS) at δ 0.00 ppm. ^{13}C NMR chemical shifts were determined relative to the signal of the solvent: $CDCl_3$ δ 77.16 ppm or CD_3OD δ 49.00 ppm. ^{19}F NMR chemical shifts were determined relative to $CFCl_3$ at δ 0.00 ppm. Chemical shifts (δ) were reported in ppm, and coupling constants were reported in Hz. The multiplicities are abbreviated as follows: s (singlet), d (doublet), t (triplet), m (multiplet), br (broad signal), dd (doublet of doublets), and so forth. High-resolution mass data were recorded on a high-resolution mass spectrometer in the ESI mode. High purities (≥95%) were also determined for all final compounds by reverse-phase HPLC (Agilent 1200). All animal studies were carried out in accordance with ethical guidelines of Emory University hospital and the First Affiliated Hospital of Jinan University.

*Synthesis of tert-butyl 4-(2-fluoro-6-(methoxycarbonyl)pyridin-3-yl)piperazine-1-carboxylate (**3**).* A round bottom flask was charged with methyl 5-bromo-6-fluoropicolinate (**1**, 234.0 mg, 1.0 mmol), *tert*-butyl 1-piperazinecarboxylate (372.6 mg, 2.0 mmol) and dissolved with 5 mL DMF. The reaction mixture was maintained at 130ºC overnight, and the progress was monitored by TLC. Upon completion, the reaction mixture was poured into 200 mL water. The aqueous phase then extracted with EtOAc (50 mL × 3). The organic phase was then combined and washed with saturated brine and dried with anhydrous Na_2SO_4. The organic phase was removed under reduced pressure, the residue was subjected to flash chromatography (Hexanes : EtOAc = 10 : 1) to yield title compound 229 mg, slight yellow solid, 68% yield. ^{1}H NMR (600 MHz, $CDCl_3$) δ 8.41 (d, J = 3.0 Hz, 1H), 8.06 (dd, J = 8.8, 1.7 Hz, 1H), 7.26 (d, J = 9.5 Hz, 1H), 3.99 (d, J = 1.7 Hz, 3H), 3.61 (t, J = 5.2 Hz, 5H), 3.40 (t, J = 5.1 Hz, 4H), 1.47 (s, 9H).

*Synthesis of 6-fluoro-5-(4-((5-fluoro-2-methyl-3-oxo-3,4-dihydroquinoxalin-6-yl)methyl)piperazin-1-yl)-N-methylpicolinamide (**5**)*. To a round bottom flask, *tert*-butyl 4-(2-fluoro-6-(methoxycarbonyl)pyridin-3-yl)piperazine-1-carboxylate (84.8 mg, 0.25 mmol) was charged and dissolved with 5 mL MeOH. Then HCl solution (2 mol/L in 1,4-dioxane, 2 mL) was injected to reaction mixture and allowed to stir under room temperature. The reaction progress was monitored by TLC. The organic solvent was removed under reduced pressure and the residue redissolved in MeCN, then 7-(bromomethyl)-8-fluoro-3-methylquinoxalin-2(1H)-one (67.8 mg, 0.25 mmol) and DIPEA (129.2 mg, 1.0 mmol, 174 mL) were added, and the reaction mixture was maintained at 80°C. The reaction progress was monitored by TLC. When starting material was consumed, the organic solvent was removed under reduced pressure. The residue was redissolved in 5 mL Ethanol and $MeNH_2$ (2 mol/L in THF, 2 mL) was added, following 12 h was applied at 80°C. After removing organic solvent, the crude product was purified by flash chromatography (EtOAc: MeOH = 10: 1), the title compound was obtained 52.5 mg, slight brown solid, 49% yield. ^{1}H NMR (600 MHz, $CDCl_3$) δ 8.41 (d, J = 3.0 Hz, 1H), 8.06 (dd, J = 8.9, 1.6 Hz, 1H), 7.26 (d, J = 9.3 Hz, 1H), 3.99 (d, J = 1.7 Hz, 3H), 3.61 (t, J = 5.2 Hz, 4H), 3.42 – 3.37 (m, 4H), 1.47 (d, J = 1.6 Hz, 10H). ^{19}F NMR (376 MHz, $CDCl_3$) δ -73.50 (d, J = 10.0 Hz). HRMS (ESI): exact mass calcd for $C_{21}H_{23}F_2N_6O_2$ ($M+H^+$), 429.18451; found, 429.18501.

Synthesis of tert-butyl 4-(2-bromo-6-(methoxycarbonyl)pyridin-3-yl)piperazine-1-carboxylate (7). A round bottom flask was charged with methyl 6-bromo-5-fluoropicolinate (**6**, 234.0 mg, 1.0 mmol), *tert*-butyl 1-piperazinecarboxylate (372.6 mg, 2.0 mmol), RuPhos-Pd (81.7 mg, 0.1 mmol, 10%), Cs_2CO_3 (651.6 mg, 2.0 mmol) and dissolved with 1,4-dioxane. The reaction mixture was maintained at 100°C for 24 h. Upon completion, the reaction mixture was poured into 100 mL water. The aqueous phase was then extracted with EtOAc (50 mL × 3). The organic phase was combined and washed with saturated brine and dried with anhydrous Na_2SO_4. The organic phase was removed under reduced pressure, the residue was subjected to flash chromatography (Hexanes : EtOAc = 10 : 1) to yield title compound 92 mg, slight yellow solid, 23% yield. ^{1}1H NMR (400 MHz, $CDCl_3$) δ 8.05 (dd, J = 8.1, 0.5 Hz, 1H), 7.30 (d, J = 8.2 Hz, 1H), 3.96 (d, J = 0.5 Hz, 3H), 3.67 – 3.60 (m, 4H), 3.14 – 3.07 (m, 4H), 1.48 (s, 9H).

*Synthesis of 6-bromo-5-(4-((5-fluoro-2-methyl-3-oxo-3,4-dihydroquinoxalin-6-yl)methyl)piperazin-1-yl)-N-methylpicolinamide (**8**).* To a round bottom flask, *tert*-butyl 4-(2-bromo-6-(methoxycarbonyl)pyridin-3-yl)piperazine-1-carboxylate (100.1 mg, 0.25 mmol) was charged and dissolved with 5 mL MeOH. Then HCl solution (2 mol/L in 1,4-dioxane, 2 mL) was injected to the reaction mixture and allowed to stir at room temperature. The reaction progress was monitored by TLC. The organic solvent was removed under reduced pressure and the residue redissolved in MeCN, then 7-(bromomethyl)-8-fluoro-3-methylquinoxalin-2(1H)-one (67.8 mg, 0.25 mmol) and DIPEA (129.2 mg, 1.0 mmol, 174 mL) were added, and the reaction mixture was maintained at 80ºC. The reaction progress was monitored by TLC. When starting material was consumed up, the organic solvent was removed under reduced pressure. The residue was redissolved in 5 mL ethanol and $MeNH_2$ (2 mol/L in THF, 2 mL) was added, following 12 h was applied at 80ºC. After removing the organic solvent, the crude product was purified by flash chromatography (EtOAc : MeOH = 10 : 1), the title compound was obtained 45.5 mg, slight brown solid, 37% yield. ^{1}H NMR (600 MHz, DMSO) δ 8.38 (t, J = 4.9 Hz, 1H), 8.17 (s, 1H), 7.91 (d, J = 8.2 Hz, 1H), 7.59 (d, J = 8.2 Hz, 1H), 7.49 (d, J = 8.3 Hz, 1H), 7.26 (t, J = 7.6 Hz, 1H), 3.68 (d, J = 6.4 Hz, 2H), 3.05 (s, 4H), 2.75 (dd, J = 4.9, 1.8 Hz, 4H), 2.62 – 2.51 (m, 3H), 2.37 (d, J = 6.8 Hz, 3H). HRMS (ESI): exact mass calcd for $C_{21}H_{23}{}^{79}BrFN_6O_2$ ($M+H^+$), 489.10444; found, 489.10478.

*Radiosynthesis of [^{18}F]**5**.* The produced [^{18}F]F^- was mixed with a solution of TEAB (tetraethylammonium bicarbonate in MeOH) (3 mg, 3.3 μmol) in a reaction vessel. After drying [^{18}F]TBAF solution at 110°C for 10 min to remove water and MeOH, three extra portions of CH_3CN were added and dried with N_2 flow at 110ºC for 3 min respectively. A solution of bromo precursor **8** (1 mg, 2.1 μmol) in anhydrous DMSO (500 μL) was then added. The vessel was heated at 170°C for 20 min. Upon completion, the reaction mixture was diluted with water (4 mL), and passed through a Sep-Pak Light C18 cartridge. The organic compounds were trapped on the cartridge, 5 mL water was used for washing, aimed to remove DMSO residue. After that, the crude product was collected by washing the cartridge with 0.5 mL CH_3CN, diluted with 4.5 mL water and then injected into a radioHPLC system. HPLC purification was performed on a Luna 5 C18(2)

100Å column (10 x 250 mm, 5 µm) using a mobile phase of CH_3CN / AMF (0.1 M) (25/75) at a flowrate of 5.0 mL/min. The retention time of [^{18}F]**5** was 16.1 min. The radioactive fraction corresponding to the desired product was collected in a sterile flask, diluted with 10 mL of water, trapped on a Sep-Pak light C18 cartridge. After washing with 10 mL of water to remove CH_3CN residue, the product was washed out from the cartridge with 0.5 mL of ethanol. The synthetic time was 80 min from end of bombardment. Radiochemical and chemical purity was measured by an analytical radioHPLC (X-Select™ HSS T3 column, 4.6 x 150 mm, 3.5 µm) using a mobile phase of CH_3CN / water (20/80 with 0.1% TEA) at a flow rate of 1 mL/min. The identity of [^{18}F]**5** was confirmed by the co-injection with unlabeled compound **5**. Radiochemical yield was 21% non-decay-corrected based on [^{18}F]F^- with >99% radiochemical purity.

ASSOCIATED CONTENT

Supporting Information

Supplemental figures and tables; Assay methods; Molecular formula string (CSV)

AUTHOR INFORMATION

Corresponding Author

Steven H. Liang − Department of Radiology and Imaging Sciences, Emory University, Atlanta, GA 30322, United States; ORCID: 0000-0003-1413-6315; Email: steven.liang@emory.edu

Authors

Xin Zhou − Department of Radiology and Imaging Sciences, Emory University, Atlanta, Georgia, 30322, United States; orcid.org/0000-0002-7444-462X

Jiahui Chen − Department of Radiology and Imaging Sciences, Emory University, Atlanta, Georgia, 30322, United States; orcid.org/0000-0001-9186-1110

Jimmy S. Patel − Department of Radiology and Imaging Sciences, Emory University, Atlanta, Georgia, 30322, United States; Department of Radiation Oncology, Winship Cancer Institute of Emory University, Atlanta, Georgia, 30322, United States; orcid.org/0000-0002-7322-7578

Wenqing Ran – Center of Cyclotron and PET Radiopharmaceuticals, Department of Nuclear Medicine & Key Laboratory of Basic and Translational Research on Radiopharmaceuticals, The First Affiliated Hospital of Jinan University, Guangzhou, 510630, China.

Yinlong Li − Department of Radiology and Imaging Sciences, Emory University, Atlanta, Georgia, 30322, United States; orcid.org/0000-0002-8864-1712

Richard S. Van – Department of Chemistry and Biochemistry, University of Oklahoma, Norman, Oklahoma 73019, United States. orcid.org/0000-0002-0185-9277

Mostafa M. H. Ibrahim – Kresge Hearing Research Institute, Department of Otolaryngology-Head and Neck Surgery, University of Michigan, Ann Arbor, Michigan, 48109, United States.

Chunyu Zhao − Department of Radiology and Imaging Sciences, Emory University, Atlanta, Georgia, 30322, United States; orcid.org/0000-0003-0168-2130

Yabiao Gao – Department of Radiology and Imaging Sciences, Emory University, Atlanta, Georgia, 30322, United States

Jian Rong − Department of Radiology and Imaging Sciences, Emory University, Atlanta, Georgia, 30322, United States; orcid.org/0000-0002-3960-1669

Ahmad F. Chaudhary − Department of Radiology and Imaging Sciences, Emory University, Atlanta, Georgia, 30322, United States.

Guocong Li – Center of Cyclotron and PET Radiopharmaceuticals, Department of Nuclear Medicine & Key Laboratory of Basic and Translational Research on Radiopharmaceuticals, The First Affiliated Hospital of Jinan University, Guangzhou, 510630, China

Junqi Hu – Center of Cyclotron and PET Radiopharmaceuticals, Department of Nuclear Medicine & Key Laboratory of Basic and Translational Research on Radiopharmaceuticals, The First Affiliated Hospital of Jinan University, Guangzhou, 510630, China.

April T. Davenport – Department of Physiology and Pharmacology, Wake Forest School of Medicine, Winston Salem, North Carolina, 27157, United States.

James D. Daunais - Department of Internal Medicine, Section on Infectious Diseases, Wake Forest School of Medicine, Winston Salem, North Carolina, 27157, United States.

Yihan Shao – Department of Chemistry and Biochemistry, University of Oklahoma, Norman, Oklahoma 73019, United States.

Chongzhao Ran – Athinoula A. Martinos Center for Biomedical Imaging, Department of Radiology, Massachusetts General Hospital and Harvard Medical School, Boston, Massachusetts, 02114, United States.

Thomas L. Collier - Department of Radiology and Imaging Sciences, Emory University, Atlanta, Georgia, 30322, United States.

Ahmed Haider − Department of Radiology and Imaging Sciences, Emory University, Atlanta, Georgia, 30322, United States; orcid.org/0000-0002-5204-4473

David M. Schuster – Department of Radiology and Imaging Sciences, Emory University, Atlanta, Georgia, 30322, United States; orcid.org/0000-0003-3077-742X

Allan Levey – Department of Neurology, Emory University, Atlanta, Georgia, 30322, United States; orcid.org/0000-0002-3153-502X

Lu Wang – Center of Cyclotron and PET Radiopharmaceuticals, Department of Nuclear Medicine & Key Laboratory of Basic and Translational Research on Radiopharmaceuticals, The First Affiliated Hospital of Jinan University, Guangzhou, 510630, China.

Gabriel Corfas – Kresge Hearing Research Institute, Department of Otolaryngology-Head and Neck Surgery, University of Michigan, Ann Arbor, Michigan, 48109, United States.

Steven H. Liang – Department of Radiology and Imaging Sciences, Emory University, Atlanta, Georgia, 30322, United States; orcid.org/0000-0003-1413-6315.

Author Contributions

All authors approved the manuscript through written contributions. X.Z., J.C., J.S.P., W.R., Y.L., R.S.V., M.M.H.I, C.Z., Y.G., J.R., A.F.C., G.L., J.H., and A.T.D. performed experiments. J.B.D., Y.S., C.R., T.L.C., A.H., D.M.S., A.L., L.W., and G.C. guided the experiments and provided suggestions. S.H.L. led the project and contributed to study conceptualization, experiment design and execution. X.Z., J.C. and J.S.P. drafted the manuscript and S.H.L. performed the final revision. All authors have given approval to the final version of the manuscript. [#]X.Z., J.C. and J.S.P. contributed equally to this work.

Notes

The authors have no conflicts of interest to declare.

ACKNOWLEDGMENTS

We thank Emory Center for Systems Imaging Radiopharmacy Core (Ronald J. Crowe, RPh, BCNP; Karen Dolph, RPh; M. Shane Waldrep) and Department of Radiology and Imaging Sciences, Emory University School of Medicine for general support. S.H.L. gratefully acknowledges the support provided, in part, by Emory Radiology Chair Fund and Emory School of Medicine Endowed Directorship. J.B.D. acknowledges the NIH grant support U01AA014106 and AA028007. J.S.P is the recipient of NCI cancer biology postdoctoral fellowship (T32CA275777).

ABBREVIATIONS

ADME, absorption, distribution, metabolism, and excretion; AMF, ammonium fluoride; AUC, area under curve; BBB, blood-brain-barrier; Boc, tert-butyloxycarbonyl; BP_{ND}, non-displaceable binding potential; Cau, caudate; Cb, cerebellum; CNS, central nervous system; Ctx, cerebral cortex; CYP, cytochrome P;

DIPEA, *N*,*N*-diisopropylethylamine; DMF, dimethylformamide; DMSO, dimethylsulfoxide; ESI, electrospray ionization; FTT, Fluorthanatrace; GBq, giga-Becquerel; Hip, hippocampus; hERG, human ether-a-go-go-related gene; HPLC, high performance liquid chromatography; MPO, multiparameter optimization; MRI, magnetic resonance imaging; MW, molecular weight; NHP, nonhuman primate; NMR, nuclear magnetic resonance; PARP, poly(ADP-ribose) polymerase; PET, positron emission tomography; PFC, prefrontal cortex; P-gp, P-glycoprotein; Pon, pons; RCY, radiochemical yield; SAR, structure−activity relationship; S_NAr, nucleophilic aromatic substitution; SRTM, simplified reference tissue model; SUV, standardized uptake value; TAC, time-activity curve; TEAB, tetraethylammonium bicarbonate; THF, tetrahydrofuran; TLC, thin layer chromatography; TPSA, topological polar surface area; WT, wild type.

REFERENCES

Uncategorized References

(1) Morales, J.; Li, L.; Fattah, F. J.; Dong, Y.; Bey, E. A.; Patel, M.; Gao, J.; Boothman, D. A. Review of poly (ADP-ribose) polymerase (PARP) mechanisms of action and rationale for targeting in cancer and other diseases. *Crit Rev Eukaryot Gene Expr* **2014**, *24* (1), 15-28. DOI: 10.1615/critreveukaryotgeneexpr.2013006875 From NLM Medline.

(2) Luo, X.; Kraus, W. L. On PAR with PARP: cellular stress signaling through poly(ADP-ribose) and PARP-1. *Genes Dev* **2012**, *26* (5), 417-432. DOI: 10.1101/gad.183509.111 From NLM Medline.

(3) Ko, H. L.; Ren, E. C. Functional Aspects of PARP1 in DNA Repair and Transcription. *Biomolecules* **2012**, *2* (4), 524-548. DOI: 10.3390/biom2040524 From NLM PubMed-not-MEDLINE.

(4) Kim, G.; Ison, G.; McKee, A. E.; Zhang, H.; Tang, S.; Gwise, T.; Sridhara, R.; Lee, E.; Tzou, A.; Philip, R.; et al. FDA Approval Summary: Olaparib Monotherapy in Patients with Deleterious Germline BRCA-Mutated Advanced Ovarian Cancer Treated with Three or More Lines of Chemotherapy. *Clin Cancer Res* **2015**, *21* (19), 4257-4261. DOI: 10.1158/1078-0432.CCR-15-0887 From NLM Medline.

(5) Ledermann, J. A. PARP inhibitors in ovarian cancer. *Ann Oncol* **2016**, *27 Suppl 1*, i40-i44. DOI: 10.1093/annonc/mdw094 From NLM Medline.

(6) Wolford, J. E.; Bai, J.; Moore, K. N.; Kristeleit, R.; Monk, B. J.; Tewari, K. S. Cost-effectiveness of niraparib, rucaparib, and olaparib for treatment of platinum-resistant, recurrent ovarian carcinoma. *Gynecol Oncol* **2020**, *157* (2), 500-507. DOI: 10.1016/j.ygyno.2020.02.030 From NLM Medline.

(7) Thapa, K.; Khan, H.; Sharma, U.; Grewal, A. K.; Singh, T. G. Poly (ADP-ribose) polymerase-1 as a promising drug target for neurodegenerative diseases. *Life Sci* **2021**, *267*, 118975. DOI: 10.1016/j.lfs.2020.118975 From NLM.

(8) Kim, C.; Chen, C.; Yu, Y. Avoid the trap: Targeting PARP1 beyond human malignancy. *Cell Chem Biol* **2021**, *28* (4), 456-462. DOI: 10.1016/j.chembiol.2021.02.004 From NLM.

(9) Curtin, N. J.; Szabo, C. Poly(ADP-ribose) polymerase inhibition: past, present and future. *Nat Rev Drug Discov* **2020**, *19* (10), 711-736. DOI: 10.1038/s41573-020-0076-6 From NLM Medline.
(10) Mao, K.; Zhang, G. The role of PARP1 in neurodegenerative diseases and aging. *FEBS J* **2022**, *289* (8), 2013-2024. DOI: 10.1111/febs.15716 From NLM Medline.
(11) Tong, J.; Chen, B.; Tan, P. W.; Kurpiewski, S.; Cai, Z. Poly (ADP-ribose) polymerases as PET imaging targets for central nervous system diseases. *Front Med (Lausanne)* **2022**, *9*, 1062432. DOI: 10.3389/fmed.2022.1062432 From NLM PubMed-not-MEDLINE.
(12) Ryu, K. W.; Kim, D. S.; Kraus, W. L. New facets in the regulation of gene expression by ADP-ribosylation and poly(ADP-ribose) polymerases. *Chem Rev* **2015**, *115* (6), 2453-2481. DOI: 10.1021/cr5004248 From NLM.
(13) Lee, Y.; Karuppagounder, S. S.; Shin, J. H.; Lee, Y. I.; Ko, H. S.; Swing, D.; Jiang, H.; Kang, S. U.; Lee, B. D.; Kang, H. C.; et al. Parthanatos mediates AIMP2-activated age-dependent dopaminergic neuronal loss. *Nat Neurosci* **2013**, *16* (10), 1392-1400. DOI: 10.1038/nn.3500 From NLM Medline.
(14) Teng, F.; Zhu, L.; Su, J.; Zhang, X.; Li, N.; Nie, Z.; Jin, L. Neuroprotective Effects of Poly(ADP-ribose)polymerase Inhibitor Olaparib in Transient Cerebral Ischemia. *Neurochem Res* **2016**, *41* (7), 1516-1526. DOI: 10.1007/s11064-016-1864-6 From NLM Medline.
(15) Xu, J. C.; Fan, J.; Wang, X.; Eacker, S. M.; Kam, T. I.; Chen, L.; Yin, X.; Zhu, J.; Chi, Z.; Jiang, H.; et al. Cultured networks of excitatory projection neurons and inhibitory interneurons for studying human cortical neurotoxicity. *Sci Transl Med* **2016**, *8* (333), 333ra348. DOI: 10.1126/scitranslmed.aad0623 From NLM Medline.
(16) Rong, J.; Haider, A.; Jeppesen, T. E.; Josephson, L.; Liang, S. H. Radiochemistry for positron emission tomography. *Nat Commun* **2023**, *14* (1), 3257. DOI: 10.1038/s41467-023-36377-4 From NLM.
(17) Willmann, J. K.; van Bruggen, N.; Dinkelborg, L. M.; Gambhir, S. S. Molecular imaging in drug development. *Nat Rev Drug Discov* **2008**, *7* (7), 591-607. DOI: 10.1038/nrd2290 From NLM.
(18) Ambur Sankaranarayanan, R.; Kossatz, S.; Weber, W.; Beheshti, M.; Morgenroth, A.; Mottaghy, F. M. Advancements in PARP1 Targeted Nuclear Imaging and Theranostic Probes. *J Clin Med* **2020**, *9* (7). DOI: 10.3390/jcm9072130 From NLM.
(19) Le Bars, D. Fluorine-18 and medical imaging: Radiopharmaceuticals for positron emission tomography. *Journal of Fluorine Chemistry* **2006**, *127* (11), 1488-1493. DOI: 10.1016/j.jfluchem.2006.09.015.
(20) Deng, X.; Rong, J.; Wang, L.; Vasdev, N.; Zhang, L.; Josephson, L.; Liang, S. H. Chemistry for Positron Emission Tomography: Recent Advances in ^{11}C-, ^{18}F-, ^{13}N-, and ^{15}O-Labeling Reactions. *Angew Chem Int Ed Engl* **2019**, *58* (9), 2580-2605. DOI: 10.1002/anie.201805501 From NLM.
(21) Matthews, P. M.; Rabiner, E. A.; Passchier, J.; Gunn, R. N. Positron emission tomography molecular imaging for drug development. *Br J Clin Pharmacol* **2012**, *73* (2), 175-186. DOI: 10.1111/j.1365-2125.2011.04085.x From NLM.
(22) Puentes, L. N.; Makvandi, M.; Mach, R. H. Molecular Imaging: PARP-1 and Beyond. *J Nucl Med* **2021**, *62* (6), 765-770. DOI: 10.2967/jnumed.120.243287 From NLM Medline.
(23) Wang, Q.; Zhang, J. Current status and progress in using radiolabelled PARP-1 inhibitors for imaging PARP-1 expression in tumours. *Eur J Med Chem* **2022**, *242*, 114690. DOI: 10.1016/j.ejmech.2022.114690 From NLM.
(24) Nguyen, N. T.; Pacelli, A.; Nader, M.; Kossatz, S. DNA Repair Enzyme Poly(ADP-Ribose) Polymerase 1/2 (PARP1/2)-Targeted Nuclear Imaging and Radiotherapy. *Cancers (Basel)* **2022**, *14* (5). DOI: 10.3390/cancers14051129 From NLM.
(25) Lee, H. S.; Schwarz, S. W.; Schubert, E. K.; Chen, D. L.; Doot, R. K.; Makvandi, M.; Lin, L. L.; McDonald, E. S.; Mankoff, D. A.; Mach, R. H. The Development of ^{18}F Fluorthanatrace: A PET Radiotracer for Imaging Poly (ADP-Ribose) Polymerase-1. *Radiol Imaging Cancer* **2022**, *4* (1), e210070. DOI: 10.1148/rycan.210070 From NLM Medline.

(26) Schoder, H.; Franca, P. D. S.; Nakajima, R.; Burnazi, E.; Roberts, S.; Brand, C.; Grkovski, M.; Mauguen, A.; Dunphy, M. P.; Ghossein, R. A.; et al. Safety and Feasibility of PARP1/2 Imaging with ^{18}F-PARPi in Patients with Head and Neck Cancer. *Clin Cancer Res* **2020**, *26* (13), 3110-3116. DOI: 10.1158/1078-0432.CCR-19-3484 From NLM Medline.
(27) Wilson, T. C.; Xavier, M. A.; Knight, J.; Verhoog, S.; Torres, J. B.; Mosley, M.; Hopkins, S. L.; Wallington, S.; Allen, P. D.; Kersemans, V.; et al. PET Imaging of PARP Expression Using ^{18}F-Olaparib. *J Nucl Med* **2019**, *60* (4), 504-510. DOI: 10.2967/jnumed.118.213223 From NLM Medline.
(28) Chen, B.; Ojha, D. P.; Toyonaga, T.; Tong, J.; Pracitto, R.; Thomas, M. A.; Liu, M.; Kapinos, M.; Zhang, L.; Zheng, M. Q.; et al. Preclinical evaluation of a brain penetrant PARP PET imaging probe in rat glioblastoma and nonhuman primates. *Eur J Nucl Med Mol Imaging* **2023**, *50* (7), 2081-2099. DOI: 10.1007/s00259-023-06162-y From NLM.
(29) Cortes Gonzalez, M. A.; Jucaite, A.; Cselenyi, Z.; Johnstrom, P.; Pike, A.; Högnäsbacka, A.; Dahl, K.; Balazs, A.; Degorce, S.; Ghosh, A.; et al. Discovery, preclinical validation and early human imaging with [^{11}C]AZ14193391 – the first blood-brain barrier permeable and subtype selective PARP1 PET radioligand. *Nucl Med Biol* **2023**, *126-127*, 108465. DOI: https://doi.org/10.1016/j.nucmedbio.2023.108465.
(30) Johnström, P.; Johannes, J.; Pike, A.; Cselényi, Z.; Schou, M. Abstract 5977: Discovery and preclinical validation of [^{11}C]AZ3391: A first in class blood-brain barrier permeable, subtype selective PARP-1 PET radioligand. *Cancer Research* **2022**, *82* (12_Supplement), 5977-5977. DOI: 10.1158/1538-7445.Am2022-5977.
(31) Staniszewska, A. D.; Pilger, D.; Gill, S. J.; Jamal, K.; Bohin, N.; Guzzetti, S.; Gordon, J.; Hamm, G.; Mundin, G.; Illuzzi, G.; et al. Preclinical Characterization of AZD9574, a Blood-Brain Barrier Penetrant Inhibitor of PARP1. *Clin Cancer Res* **2023**. DOI: 10.1158/1078-0432.CCR-23-2094 From NLM Publisher.
(32) Waterhouse, R. N. Determination of lipophilicity and its use as a predictor of blood-brain barrier penetration of molecular imaging agents. *Mol. Imaging Biol.* **2003**, *5*, 376-389, Review.
(33) Pike, V. W. Considerations in the development of reversibly binding PET radioligands for brain imaging. *Curr. Med. Chem.* **2016**, *23* (18), 1818-1869, Review.
(34) Chen, Z.; Chen, J.; Chen, L.; Yoo, C. H.; Rong, J.; Fu, H.; Shao, T.; Coffman, K.; Steyn, S. J.; Davenport, A. T.; et al. Imaging Leucine-Rich Repeat Kinase 2 In Vivo with ^{18}F-Labeled Positron Emission Tomography Ligand. *J Med Chem* **2023**, *66* (3), 1712-1724. DOI: 10.1021/acs.jmedchem.2c00551 From NLM.
(35) Johannes, J. W.; Balazs, A.; Barratt, D.; Bista, M.; Chuba, M. D.; Cosulich, S.; Critchlow, S. E.; Degorce, S. L.; Di Fruscia, P.; Edmondson, S. D.; et al. Discovery of 5-{4-[(7-Ethyl-6-oxo-5,6-dihydro-1,5-naphthyridin-3-yl)methyl]piperazin-1-yl}-N-methylpyridine-2-carboxamide (AZD5305): A PARP1-DNA Trapper with High Selectivity for PARP1 over PARP2 and Other PARPs. *J Med Chem* **2021**, *64* (19), 14498-14512. DOI: 10.1021/acs.jmedchem.1c01012 From NLM.
(36) Wang, Z. Q.; Auer, B.; Stingl, L.; Berghammer, H.; Haidacher, D.; Schweiger, M.; Wagner, E. F. Mice lacking ADPRT and poly(ADP-ribosyl)ation develop normally but are susceptible to skin disease. *Genes Dev* **1995**, *9* (5), 509-520. DOI: 10.1101/gad.9.5.509 From NLM.
(37) Zhang, X.; Zhang, Y.; Chen, Z.; Shao, T.; Van, R.; Kumata, K.; Deng, X.; Fu, H.; Yamasaki, T.; Rong, J.; et al. Synthesis and preliminary studies of ^{11}C-labeled tetrahydro-1,7-naphthyridine-2-carboxamides for PET imaging of metabotropic glutamate receptor 2. *Theranostics* **2020**, *10* (24), 11178-11196. DOI: 10.7150/thno.42587.
(38) Yu, Q.; Kumata, K.; Rong, J.; Chen, Z.; Yamasaki, T.; Chen, J.; Xiao, Z.; Ishii, H.; Hiraishi, A.; Shao, T.; et al. Imaging of Transmembrane AMPA Receptor Regulatory Proteins by Positron Emission Tomography. *J Med Chem* **2022**, *65* (13), 9144-9158. DOI: 10.1021/acs.jmedchem.2c00377 From NLM.
(39) Note_PARP1_Allen_brain_atlas. PARP1 expression available at The Allen Brain Atlas database, see: https://mouse.brain-map.org/gene/show/11332. **2023**.